Applied Energy 288 (2021) 116603

Contents lists available at ScienceDirect

Applied Energy

journal homepage: www.elsevier.com/locate/apenergy

Performance analysis of evacuated solar thermal panels with an infrared mirror

Carmine D'Alessandro [a,b], Davide De Maio [a,b], Marilena Musto [a,b], Daniela De Luca [c,b,*], Emiliano Di Gennaro [c,b], Peter Bermel [d], Roberto Russo [b]

[a] Industrial Engineering Department, University of Napoli "Federico II", Napoli, Italy
[b] Consiglio Nazionale delle Ricerche, Istituto di Scienze Applicate e Sistemi Intelligenti, 80131 Napoli, Italy
[c] Physics Department, Università degli Studi di Napoli "Federico II", 80125 Napoli, Italy
[d] School of Electrical and Computer Engineering, Birck Nanotechnology Center, Purdue University, West Lafayette, IN 47906, USA

GRAPHICAL ABSTRACT

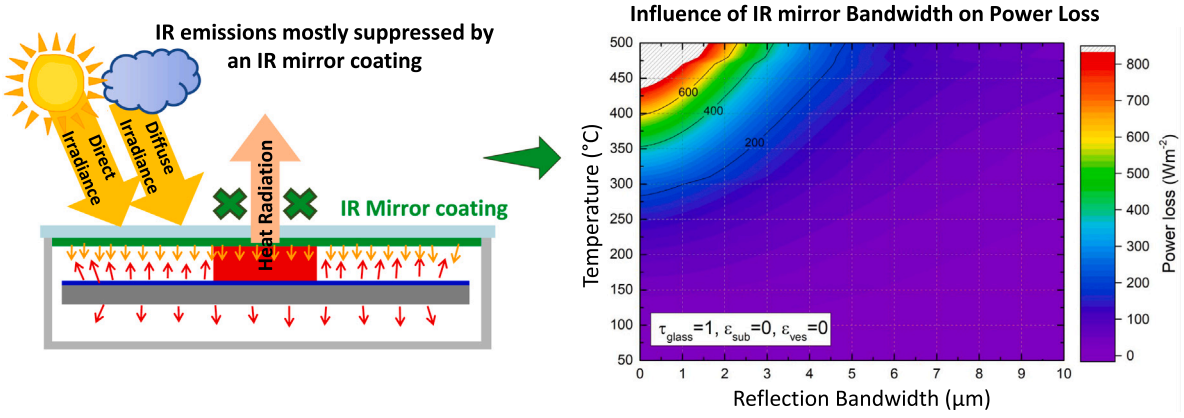

ARTICLE INFO

Keywords:
IR mirror
Solar energy
Photon recycling
Thermal analysis
High vacuum flat panel

ABSTRACT

Reducing thermal losses in solar thermal devices is fundamental for enhancing conversion efficiencies, particularly at high operating temperatures. In this work, we consider the benefits of adding an InfraRed (IR) mirror coating to the inner surface of the glass encapsulating a High Vacuum insulated Flat plate solar thermal Panel (HVFP). The IR mirror helps recover the radiation emitted by the absorber by sending it back to the absorber itself. This mechanism, known as cold-side external photon recycling, allows a reduction of radiative losses and, consequently, an improvement of the panel efficiency. The performance of the structure presented in this manuscript is studied via a thermal model. A detailed discussion on the increasing efficiency is presented, and results are presented by taking into account different parameters, like the mirror transparency, reflectivity and reflection bandwidth, as well as different operating temperatures of the panel. Finally, the annual energy gain associated with the IR mirror is analyzed in the case of three different cities, using historical data, showing that improvement higher than 50% can be obtained at operating temperatures above 300 °C.

* Corresponding author at: Physics Department, Università degli Studi di Napoli "Federico II", 80125 Napoli, Italy.
E-mail address: daniela.deluca@unina.it (D. De Luca).

https://doi.org/10.1016/j.apenergy.2021.116603
Received 22 October 2020; Received in revised form 25 January 2021; Accepted 1 February 2021
Available online 17 February 2021

Nomenclature

Abbreviations and subscripts

abs	Absorber
all	Overall
amb	Ambient
BB	Blackbody
C	Solar concentration
c	Collector
CSP	Concentrating solar power
cut	Cut-off
HVFP	High vacuum insulated flat plate solar thermal panel
I	Solar irradiance, W m^{-2}
IR	Infrared
IRM	Infrared mirror
MT-SSA	Mid-temperature selective solar absorber
q	Power loss, W m^{-2}
SSA	Selective solar absorber
sub	Substrate
T	Temperature, K
thres	Threshold
vess	Vessel

Greek Symbols

α	Absorptance
$\bar{\alpha}$	Spectrally averaged solar absorptivity
$\bar{\varepsilon}$	Spectrally averaged thermal emissivity
Δ	Bandwidth, μm
η	Efficiency
λ	Wavelength, μm
ρ	Reflectivity
σ	Stefan–Boltzmann constant, W m^{-2} K^{-4}
τ	Transparency
ε	Emissivity

1. Introduction

Over the past few decades, sustainable energy has played an increasingly important role in reducing global warming and the need for fossil fuels [1]. Solar power, in particular, draws from an abundant source, large enough to supply all global energy needs [2,3]. While solar photovoltaics are widely used to capture this resource, solar thermal technologies that capture sunlight as heat also help decrease environmental pollution by providing a renewable heat resource that can be used either directly or as a means for power generation [4].

Solar thermal devices are mainly divided into two categories: Concentrator and Flat Plate Solar Thermal devices [5], both used in several applications, mainly in the industrial field. Concentrators enable high temperature outputs; they mainly collect direct solar radiation and a small portion of the diffuse rays that fall within the acceptance angle. The tracking infrastructure can also add to the expense and complication of the devices themselves. From this perspective, flat plate systems may appear to be more versatile, since they are able to collect both diffuse and direct rays, and cheaper, since they do not need solar tracking.

However, flat plates are not currently used in applications requiring temperature heat higher than 180 °C, since they often experience relatively low temperature outputs and high losses, caused by the three heat transfer processes: conduction, convection and radiation. Even if high-vacuum insulation suppresses the first two components, the radiative term still survives, and rises rapidly with temperature, particularly in the absence of concentration [6]. This limits the use of flat panel devices at these temperatures, since they experience a fast drop off in the radiative efficiency of the absorber η, defined as [7]:

$$\eta = \bar{\alpha} - \frac{\bar{\varepsilon}(T)\sigma T^4}{C I}, \tag{1}$$

where C is the solar concentration, σ is the Stefan–Boltzmann constant, T is the operating temperature, I is the solar irradiance, and $\bar{\alpha}$ and $\bar{\varepsilon}$ are the spectrally averaged solar absorptance and thermal emittance, respectively. In Eq. (1), all the surrounding elements are considered to operate near room temperature, which allows their contributions to the efficiency to be neglected. Instead, this expression highlights the leading role of two factors that contribute to the device efficiency: the solar absorptance and the thermal emittance.

Therefore, for flat plate applications, non-selective absorbers must be replaced by a spectrally-Selective Solar Absorber (SSA) [8,9], characterized by absorptance $\alpha \sim 1$ in the region where the Solar spectrum has its maximum intensity (i.e. 0.3–2.0 μm) and emittance $\varepsilon \sim 0$ for longer wavelengths. SSAs have been extensively studied since '50s, and several materials have been explored during the years: multilayered structures [10,11], high entropy alloy [12], cermets (metal–dielectric composites) [13,14], inherently selective materials [15], semiconductor–metal tandems [16,17], textured materials [18,19], photonic designs [20,21], and plasmonic designs [22,23].

While improved thermal efficiency can be easily reached with SSAs, increasing their operating temperature can cause challenges with stability and large scale production [7,24], particularly in HVFP collectors, where high thermal conductivity substrates, such as copper or aluminum, are required. Part of the reason is that many materials experience phase changes and/or shifts in their dispersion with temperature. In the case of metals, often the Drude conductivity drops, resulting in higher IR emission.

One of most functional and easy-to-fabricate SSAs is the multilayer design: a recent work [25] has demonstrated that with a simple Cr_2O_3/Ti/Cr_2O_3 tri-layer design, the SSA can reach an efficiency more than double that of a commercially available absorber [26] at temperatures up to 300 °C, 48% Vs 20%.

Despite its strong selectivity, the SSA still experiences radiative losses ($\varepsilon \neq 0$ in the near-IR). There, a second route could be followed: cold-side external photon recycling. In fact, since radiation exchange takes place between the absorber and the glass encapsulation, this suggests that, using a properly designed IR mirror, one could recapture the infrared emissions by reflecting them back to the absorber itself.

Such IR mirrors may have important applications in solar, thermal and electric conversion, as well as solar heating and solar photovoltaic conversion. The influence of the use of IR mirrors has already been deeply studied for concentrators. Prior work [27] has demonstrated how an IR-reflective cover coated on the dark side of the receiver tube can bring a gain in efficiency over a year comparable to the one obtained with an AR treatment. Also, [28,29] pointed out the versatility of such mirror, which can be used both as an alternative to selective coatings, and in an hybrid system, i.e. by taking advantage of the selective coating on the absorber pipe on the lower temperature section of the receiver, and of the hot mirror coating in the high temperature sections. The reason is that the glass cover remains cooler, and thus experiences less thermal expansion-driven mechanical stress.

All these prior publications are based on numerical models, which do not include any spectral analysis of the system; they use just one numerical value for solar transmissivity and one for IR reflectivity, although fabricated reflectors have finite bandwidths for each behaviors. For a deeper and more accurate analysis, the wavelength dependence of reflectivity and transmissivity must be properly taken into account. We therefore want to extend those results to include the case of the HVFP produced by TVPSolar [30], where, in addition, guaranteeing

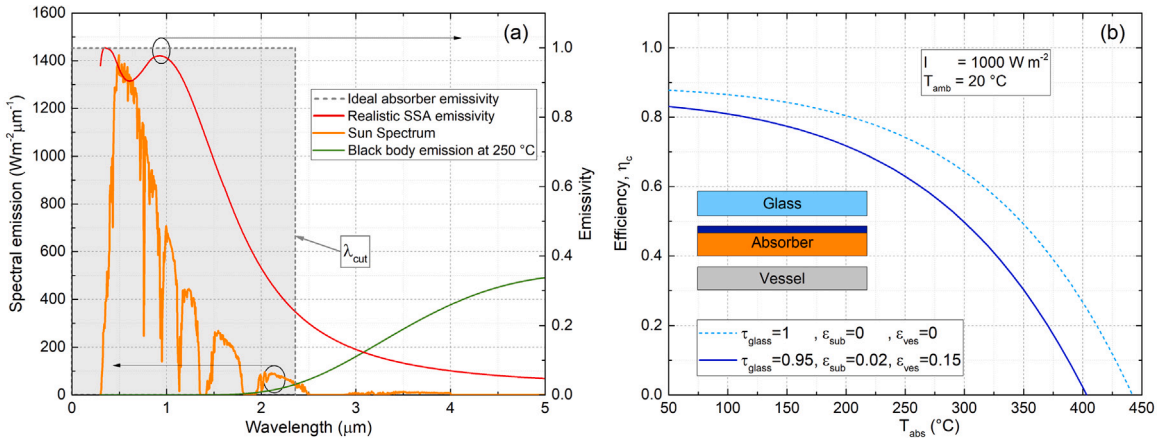

Fig. 1. (a) Left-hand axis: Solar spectral emission at the Earth surface (orange line) and blackbody emission at 250 °C (green line). Right-hand axis: emissivity curve of an ideal absorber (gray dashed line ending at λ_{cut}) and an optimized absorber (red line). (b) Calculated absorber efficiency (cyan dashed line) and HVFP efficiency (blue solid line) as a function of absorber temperature. Inset: schematic cross view (not to scale) of our system.

a high transparency in the visible region is crucial to avoid altering the absorber performance. Fortunately, a prior experimental work on incandescent light source [31] has showed that both recycling of the infrared radiation and transmission of the visible light are allowed, thus tripling the system overall efficiency.

Ideally, the perfect mirror is characterized by a transparency, τ_{IRM}, close to 1 in the visible and near-IR regions and a reflectivity, ρ_{IRM}, almost equal 1 in the mid-IR region: in this way it allows virtually all incident solar power to reach the absorber, while reflecting nearly all the power re-emitted back to the absorber itself [32]. However, an IR mirror with such ideal properties is challenging to fabricate experimentally, and undesired reflections and absorption peaks could emerge along the spectrum.

It has previously been demonstrated that changing the reflectivity values of the inner surface of the cavity lead to different temperatures and efficiencies [33]. For this reason, thermal simulations are fundamental to understand what minimum spectrally-averaged transparency and reflectivity values are needed to produce significant gains in efficiency under different conditions. In this work, we aim to address this gap by investigating the fundamental principles of an effective IR mirror design, which allows for the potential non-idealities associated with creating a real design with a finite number of layers, made from materials with absorption and dispersion, as well as geometries with limited reflection bandwidths, and wavelength-dependent reflectivity values.

To address these questions, this manuscript is structured as follows: in Section 2, we show details of our methodology for simulating the performance of a HVFP with an IR mirror coated on the inner face of the glass encapsulating the panel. Then, in Section 3, we present the main results obtained by means of thermal simulations. Finally, we conclude by summarizing our findings and proposing new perspectives in Section 4.

2. Methodology

The HVFP under study consists of an SSA coated on a copper substrate and enclosed between a highly transparent glass cover and a stainless steel vessel. For simplicity, we assume that the glass–absorber and absorber–vessel distances are much smaller than the lateral widths of each, allowing the system to behave much like three effectively infinite layers, as schematically represented in the inset of Fig. 1(b). The thermal exchanges can be effectively described by the equation of radiative exchange between flat parallel plates in a 1D thermal model that neglects thermal gradient and boundary effects, as experimentally demonstrated in [34]. In addition, the glass cover could be coated on the inner side by an IR mirror to reduce the absorber radiation losses (see inset of Fig. 3): in the next section, we will discuss in detail the impact of such a mirror on the overall performance of the HVFP. Since we expect the results to be strongly dependent on the absorber spectral emissivity, we investigate the performance of the discussed structure in the particular case of an HVFP equipped with an SSA optimized for Mid-Temperature operation (MT-SSA). In the following, we describe the steps needed to evaluate the effect of an IR mirror on the HVFP efficiency, comparing two different scenarios: one in which the absorber loses thermal power only through irradiation ($\bar{\varepsilon}_{sub} = 0$, $\bar{\varepsilon}_{vess} = 0$, and τ_{glass}=1), and one in which the whole collector is considered, where both the radiative exchange with the vessel and the non-ideal glass transparency are included ($\bar{\varepsilon}_{sub} = 0.02$, $\bar{\varepsilon}_{vess} = 0.15$, and τ_{glass}= 0.95).

2.1. Ideal SSA

An ideal SSA exhibits an absorptivity curve like the gray dashed line in Fig. 1(a): $\alpha(\lambda) = 1$ where $\lambda < \bar{\lambda}$, being $\bar{\lambda}$ the transition wavelength from high-to-low absorptivity. One can easily calculate its efficiency using Eq. (1); its value depends greatly on the SSA temperature (T_{abs}) and its spectral features ($\bar{\lambda}$). Fig. 1(a) shows the blackbody emission at 250 °C (green line) and the solar spectral emission at the Earth surface (orange line). The latter behaves like a blackbody at a temperature of 5500 K, with some near-zero intensity regions due to the light absorption in the atmosphere. In accordance with this temperature-dependent character of the blackbody emission, the cut-off wavelength $\lambda_{cut}(T_{abs})$ is defined as the transition wavelength that maximizes the efficiency at T_{abs} (as calculated in Eq. (2)). Generally, this transition occurs at the wavelength where the blackbody emission exceeds the incident solar radiation [13].

Calculating the overall efficiency of the system requires implementing an energy balance calculation in thermal equilibrium. In particular, the presence of the absorber substrate, the glass, and the vessel needed to realize the high vacuum environment must also be considered. By including extra-transparent glass with a double AR coating and transparency $\tau = 0.95$, a copper substrate with $\bar{\varepsilon}_{sub} = 0.02$ and a stainless steel vessel with $\bar{\varepsilon}_{vess} = 0.15$, the overall efficiency decreases, as shown in Fig. 1(b). In this case, the efficiency calculation is based on Eq. (4), which will be described in detail in Section 2.4, where $I = 1000\,\mathrm{W/m^2}$ and a room temperature of 20 °C have been considered.

2.2. Realistic SSA

To mimic the response of an ideal SSA, we used an alternating dielectric–metal multilayered structure (Cr_2O_3/Ti/Cr_2O_3) deposited on

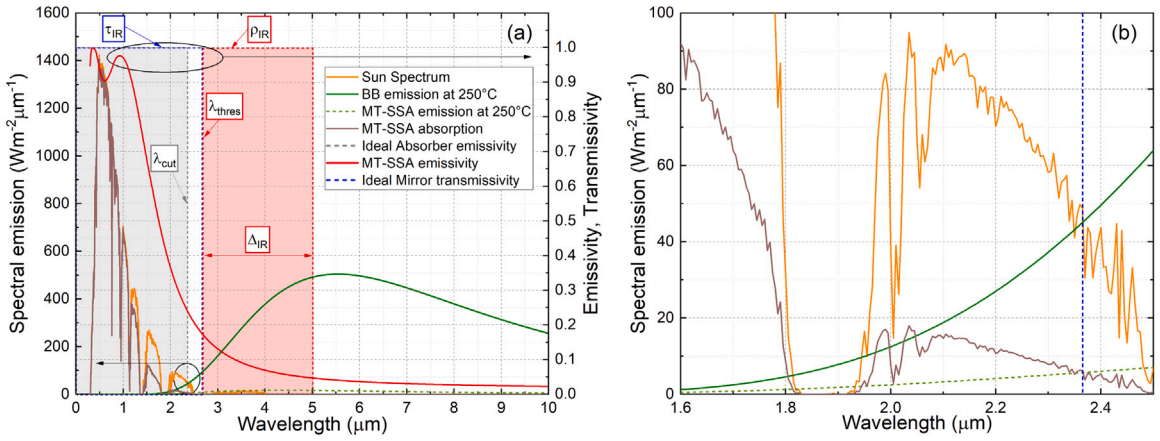

Fig. 2. (a) Left-hand axis: Solar spectral emission at the Earth surface (orange line) compared with the blackbody emission at 250 °C (green line), the MT-SSA absorption (dark brown line) and emission (green dashed line) at 250 °C. Right-hand axis: emissivity of ideal SSA (gray dashed line), realistic SSA (red solid line); transmissivity (blue dashed line) and reflectivity (red dashed line) of an ideal IR mirror. (b) Enlarged view of the wavelength region where the emission and absorption curves cross.

a copper substrate. By means of optical simulations and an optimization procedure originally presented in [25], we show that its emissivity curve can be adjusted to partially fit a target function by varying the layer thicknesses, preserving a high solar absorption and reducing the thermal emission. In Fig. 2(a), the emissivity curve of our MT-SSA (red line) is compared with the same curve for an ideal SSA (gray dashed line), both designed to work at 250 °C (λ_{cut} = 2.35 μm for both). As evident, the response of the real structure is not able to reproduce the steepness of the ideal one at λ_{cut}, nonetheless such MT-SSA has $\bar{\alpha} = 0.88$ and a spectrally averaged emissivity $\bar{\varepsilon} = 0.035$ at 250 °C.

2.3. MT-SSA and ideal IR mirror

To further reduce the radiative losses of our MT-SSA in HVFP, it is crucial to recycle all or at least part of the power lost as thermal radiation, by reflecting it back to the absorber. We consider here the contribution of an additional layer made of an ideal material, assumed to perfectly reflect the absorber radiation in a well-defined region of the spectrum, and perfectly transparent elsewhere. This layer, placed on the inner side of the cover glass, operates at room temperature and hence has a very low emission. The absorber, when operating at 250 °C, for instance, presents an emission spectrum described by the green dotted line in Fig. 2(a) and (b), which is determined by the product of the blackbody emission (green dashed line) and its emissivity curve (red dashed line) and has non-negligible values in the IR region between 1 and 10 μm. We require that our ideal material acts as an IR mirror coating and is characterized by a spectral reflectivity $\rho_{IRM} = 1$ throughout this IR region (highlighted by the red rectangle in Fig. 2(a)) and transparency $\tau_{IRM} = 1$ where the solar spectrum is maximal (visible and near-IR regions). Again, the transition from high transparency to high reflectivity happens at a specified wavelength, which we call λ_{thres}. Similarly to λ_{cut}, λ_{thres} is defined as the shorter wavelength with $\rho_{IRM} = 1$. Moreover, to adhere to experimental constraints, we only considered limited reflection bandwidths, Δ_{IRM}.

Therefore, the radiative efficiency of an ideal system including only a glass, a mirror, and an absorber, η_{abs}, can be defined in terms of absorbed, emitted and incident power as follows:

$$\eta_{abs} = \frac{P_{absorbed} - P_{emitted}}{P_{incident}} = \\ = \frac{\int_{\lambda_1}^{\lambda_2} \varepsilon_{abs}(\lambda) I(\lambda) d\lambda - \int_0^{\infty} \varepsilon_{abs-glass}(\lambda)[E_{BB}(\lambda, T_{abs}) - E_{BB}(\lambda, T_{amb})] d\lambda}{\int_{\lambda_1}^{\lambda_2} I(\lambda) d\lambda}, \quad (2)$$

where λ is the electromagnetic wavelength, T_{abs} is the absorber temperature, $I(\lambda)$ is the solar spectral irradiance, $E_{BB}(\lambda, T_{abs})$ is the blackbody spectral emission calculated at the absorber temperature value. λ_1 = 0.25 μm and λ_2 = 2.5 μm represent the lower and the higher limits of the solar region, respectively, $\varepsilon_{abs}(\lambda)$ is the spectral emissivity of the absorber, and $\varepsilon_{abs-glass}(\lambda)$ is the equivalent emissivity of the absorber facing the glass, calculated as a $0-D$ equation of the radiative heat transfer [35]:

$$\varepsilon_{abs-glass}(\lambda) = \frac{1}{\frac{1}{1-\rho_{IRM}(\lambda)} + \frac{1}{\varepsilon_{abs}(\lambda)} - 1}. \quad (3)$$

Note that $\varepsilon_{abs-glass}(\lambda)$ reduces to $\varepsilon_{abs}(\lambda)$ if $\rho_{IRM}(\lambda) = 0$, whereas $\varepsilon_{abs-glass}(\lambda) = 0$ for $\rho_{IRM}(\lambda) = 1$, meaning that the ideal mirror reflects all the photons emitted by the absorber back to itself. In the analyzed system the power loss is $q_L = \bar{\varepsilon}_{abs-glass}(T)\sigma(T_{abs}^4 - T_{amb}^4)$, where $\bar{\varepsilon}_{abs-glass}(T)$ is the spectral averaged emissivity of the system. Therefore, according to Eq. (3), the regions where $(1 - \rho_{IRM}(\lambda)) \lesssim \varepsilon_{abs}(\lambda)$ reduce $\bar{\varepsilon}_{abs-glass}(T)$ and, consequently, the power loss.

Eqs. (2) and (3) are derived in the particular case of infinite parallel plates, but they represent a good approximation of the absorber efficiency, since in the evacuated flat collector the distance between the glass and the absorber is two orders of magnitude lower than the absorber size. By using Eq. (2), it is possible to define the ideal λ_{thres} as the wavelength that maximizes the absorber efficiency at a given temperature.

2.4. Real IR mirror

From an experimental point of view, realizing an ideal IR mirror is not an easy task. It can be produced by using a rugate filter design, which consists of alternating layers of dielectric materials and, to best suppress high order harmonics due to a large variation of the refractive index values of two adjacent layers, a continuous and sinusoidal variation of the refractive index as a function of optical thickness is required [36]. While one can readily obtain a near-ideal mirror for a relatively small bandwidth [37,38], transmissivity and reflectivity may deviate much more from the ideal as the bandwidth is increased substantially. Therefore, since an infinitely wide reflection window and high transparency in the solar region cannot be simultaneously realized in experiment, the range of reflected wavelengths must be bounded. For this reason, we introduced a new parameter, Δ_{IRM}, which represents the high-reflection window width, such that the IR mirror has nearly ideal behavior only in a finite region: it has a fixed starting point, $\lambda_{thres}(T)$, but a variable ending point, $\lambda_{thres} + \Delta_{IRM}$. Outside the range $[\lambda_{thres}, \lambda_{thres} + \Delta_{IRM}]$, the IR mirror coating is supposed to be perfectly transparent, showing the cover glass with the typical emissivity $\varepsilon_{glass} = 0.89$ (see Fig. 2). To reach a configuration that can actually be experimentally produced by using a realistic set of materials, we need to consider further constraints:

- solar transparency $\tau_{IRM} < 1$ below λ_{thres};
- reflectivity $\rho_{IRM} < 1$ over the range $[\lambda_{thres}, \lambda_{thres} + \Delta_{IRM}]$.

Note that, to obtain the overall solar transparency value, one should multiply the mirror transparency, τ_{IRM}, by the one of the glass, τ_{glass}, i.e. $\tau_{all} = \tau_{glass} \times \tau_{IRM}$. Of course, this non-ideality have to be taken into account in calculating the overall collector efficiency, as we will see in the next subsection.

2.5. Collector efficiency

To calculate the overall efficiency of an evacuated flat collectors more terms have to be included: the glass transparency and the substrate and vessel emissivities. The finite bandwidth, Δ_{IRM}, and the reflectivity values $\rho_{IRM} < 1$ over the range $[\lambda_{thres}, \lambda_{thres} + \Delta_{IRM}]$ can be easily taken into account in Eq. (2) and (3) by assuming the proper values for $\rho_{IRM}(\lambda)$. Therefore, the analytical formula for the collector efficiency calculation, η_c, based on the described $0-D$ thermal model, becomes:

$$\eta_c = \frac{\int_{\lambda_1}^{\lambda_2} \tau_{glass}\tau_{IRM}(\lambda)\varepsilon_{abs}(\lambda)I(\lambda)d\lambda - \int_0^{\infty} \varepsilon_{all}(\lambda)[E_{BB}(\lambda, T_{abs}) - E_{BB}(\lambda, T_{amb})]d\lambda}{\int_{\lambda_1}^{\lambda_2} I(\lambda)d\lambda} \tag{4}$$

where

$$\varepsilon_{all} = \varepsilon_{abs-glass} + \varepsilon_{sub-vess} \tag{5}$$

and

$$\varepsilon_{sub-vess}(\lambda) = \frac{1}{\frac{1}{\varepsilon_{sub}(\lambda)} + \frac{1}{\varepsilon_{vess}(\lambda)} - 1}, \tag{6}$$

which describes the thermal loss due to the substrate of the absorber that faces the interior side of the vessel. The emissivity values of the stainless steel vessel and the copper substrate are subsequently assumed to be 0.15 and 0.02, respectively. In the previous formula we assumed that both glass and vessel remain at room temperature. This is not a risky assumption, in fact it has been experimentally observed that, when in operation, both the glass and the vessel of an HVFP do not exceed T_{amb} by more than 10 °C. The mathematical model describing the collector efficiency as in Eq. (4) has been validated, in the absence of the IR mirror, by numerical simulations performed using COMSOL Multiphyics [39] and an experimental system [25].

3. Results

In the following, we show the relevant results of our analysis divided in different sub-sections, starting from the definition of λ_{cut} and λ_{thres} to the annual energy output.

3.1. MT-SSA and ideal IR mirror: results

In Fig. 3, the optimal values of $\lambda_{cut}(T)$ are provided as a function of temperature (empty black square). $\lambda_{cut}(T)$ is determined by maximizing the efficiency of the ideal SSA described by Eq. (2), to absorb as much sunlight as possible while reradiating as little IR radiation as possible. It only depends on the operating temperature and solar concentration, therefore its value cannot be influenced by the presence of the IR mirror ($\rho_{IRM}(\lambda) = 0$ in Eq. (3)). Note that the zero intensity regions in the solar spectrum at the Earth surface is responsible for the stepped behavior of λ_{cut} [13].

Once we determine $\lambda_{cut}(T)$, we can then calculate the $\lambda_{thres}(T)$ values (red circles in Fig. 3) by maximizing the efficiency of a collector equipped with an SSA having the chosen λ_{cut} and the ideal IR mirror facing the absorber: Eq. (2) has been used and $\rho_{IRM}(\lambda) = 1$ has been fixed for each $\lambda > \lambda_{thres}(T)$. The value of $\lambda_{thres}(T)$ and $\lambda_{cut}(T)$ perfectly overlap in the whole range of considered temperatures, showing that

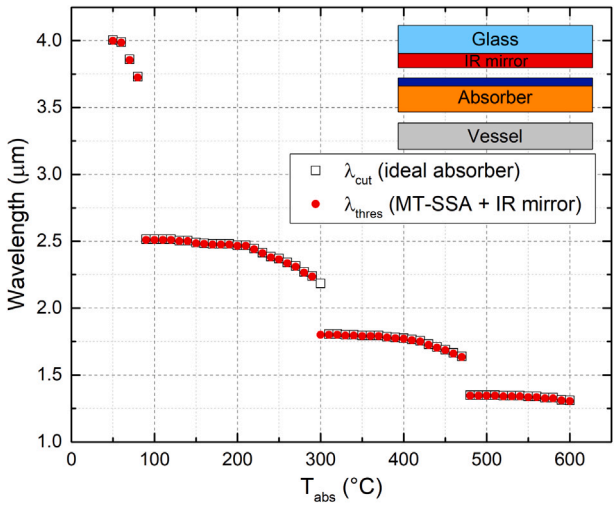

Fig. 3. The cut-off wavelength, λ_{cut}, for the ideal absorber and threshold wavelength, λ_{thres}, for a realistic SSA combined with the ideal IR mirror are compared at different working temperatures. The inset shows the system described in Fig. 1, where an IR mirror on the inner side of the glass has been added (red layer).

$\lambda_{thres}(T)$ does not depend on the optical properties of the absorber. The reason is that for $\lambda < \lambda_{thres}$, the absorber spectral emissivity calculated at the specific working temperature affects solar absorption and radiative emission in the same way (see Fig. 2b), whereas for $\lambda > \lambda_{thres}$ the ideal absorber also behaves as an ideal IR mirror.

We therefore fix $\lambda_{thres}(T)$ to the values reported in Fig. 3 and assume a finite width of the IR mirror to calculate the efficiency of our MT-SSA. The mirror is assumed to be ideal, i.e. reflectivity equals 1 from $\lambda_{thres}(T)$ to $\lambda_{thres}(T) + \Delta_{IRM}$ and transparency equals 1 outside this region (see Fig. 2a).

3.2. Ideal IR mirror: results

The calculated power losses are reported in Fig. 4(a) for the absorber–glass system alone, and in Fig. 4(b) for the whole collector. $\Delta_{IRM} = 0$ corresponds to the power loss calculated in absence of the IR mirror. The presence of an ideal IR mirror ($\Delta_{IRM} > 0$) keeps power losses low even for absorber temperatures higher than 250 °C; for example, only $200\,W\,m^{-2}$ are lost at 325 °C when an ideal mirror with $\Delta_{IRM} = 2\,\mu m$ is used. In Fig. 4(b), the addition of the radiative losses from both the substrate and the vessel reduces the absorber stagnation temperature from 450 °C to 405 °C at $I = 1000\,W\,m^{-2}$: the patterned area represents the region where the power loss is higher than the absorbed power.

An additional small contribution to the power loss is due to the substrate emissivity towards the vessel. This could also be recovered if an additional coating is applied to the stainless steel vessel. In this case, there is no need for transparency, so the coating could be made of silver, which has a $\rho = 0.99$ in IR [40].

The reduced power losses directly increase the efficiency. In Fig. 5, we report the efficiency change ($\Delta\eta$), defined as the difference between the efficiency with and without the IR mirror at $I = 1000\,W\,m^{-2}$ and $T_{amb} = 20°C$. It has been calculated for the absorber alone (η_{abs}, Fig. 5(a), or for the whole collector (η_c, Fig. 5(b)).

As expected, the broader the IR window, the bigger the efficiency change. However, a reflection bandwidth of two micrometers is already enough to produce an absolute efficiency change of 0.1 at 325 °C. The efficiency change is more pronounced when the absorber temperature increases, reaching a maximum of 0.70 close to the stagnation temperature of the absorber–glass system.

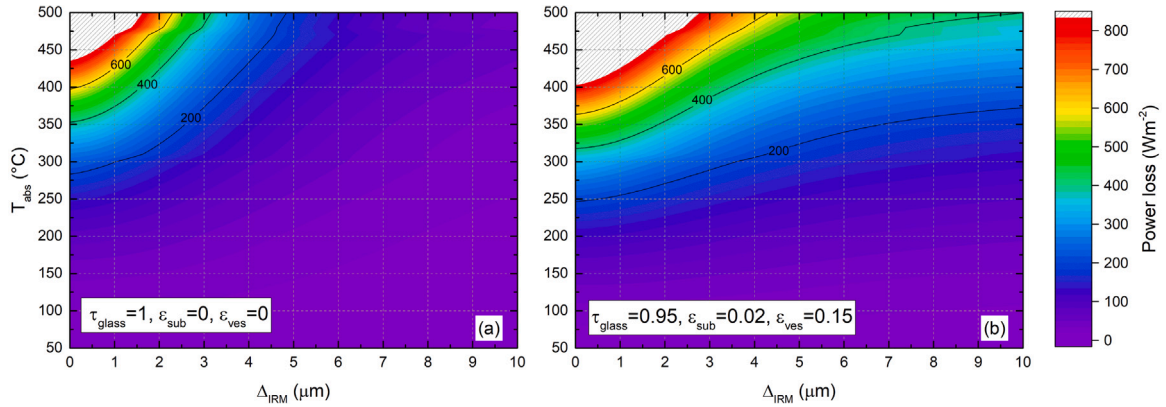

Fig. 4. Effect of an ideal IR mirror on the power loss of (a) an MT-SSA absorber and (b) an HVFP collector equipped with an MT-SSA, as a function of the working temperature and of Δ_{IRM}.

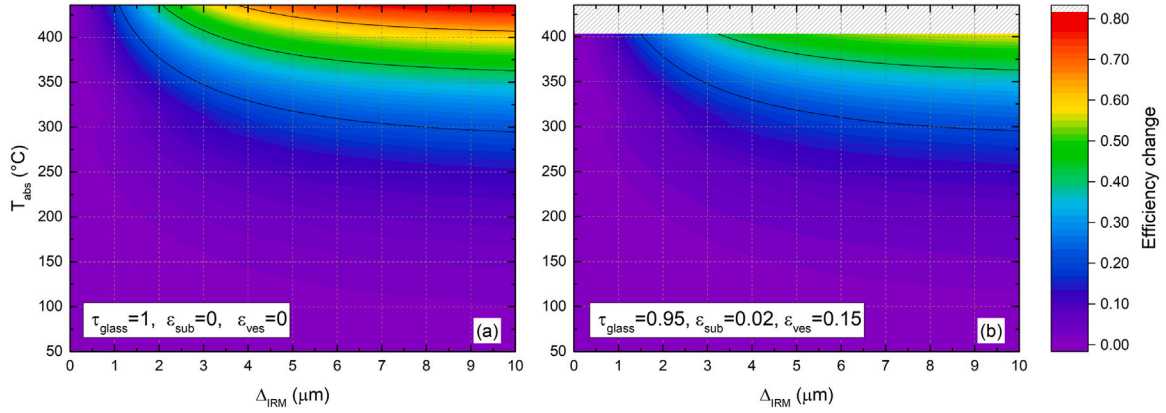

Fig. 5. Efficiency change trend as a function of working temperature and Δ_{IRM} for (a) the MT-SSA alone and (b) the HVFP collector equipped with an MT-SSA.

Because of the additional losses shown in Fig. 4(b), a slight reduction in the MT-SSA stagnation temperature (from 450 °C to 405 °C) is evident in Fig. 5(b). Above this temperature, the efficiency is not well defined, and $\Delta\eta$ cannot be calculated. This region is represented as the patterned area.

To highlight the effect of the cold-side external photon recycling on the panel performance, we compare the available power, i.e the power converted into heat by the absorber in presence of the IR mirror and defined as $\eta \times I(\lambda)$, with the recovered power, defined as $\Delta\eta \times I(\lambda)$. The analysis has been performed for different absorber working temperatures and results are shown in Fig. 6, for the system absorber–glass (a) or for the whole collector (b). By comparing the two cases, it is evident that the presence of the substrate and vessel only changes the available power, since the power losses due to the substrate are not recovered in the present configuration. Moreover, the case $\Delta_{IRM} = 0$ corresponds to the absence of the mirror, therefore the recovered power (solid lines) is zero. By increasing the Δ_{IRM}, the IR mirror acts as a photon recycler, contributing to the increasing of efficiency: the recovered power increases and sum up to the power converted by the absorber alone, increasing the available power to levels which are very close to the ideal one ($\bar{\alpha} \times \tau_{glass} \times \tau_{IRM} \times I$). Also, since the emitted power increases with temperature, the recovered power will increase too.

The results in Fig. 6 indicate that, after a quite rapid increase, by increasing the Δ_{IRM} the recovered power saturates. This can be understood by looking at the emissivity curve of MT-SSA reported in Fig. 2 that shows how this emissivity becomes smaller when increasing the wavelength. The power emitted by a blackbody at 250 °C has a maximum around 5.5 μm, and decreases at larger wavelength, where also the spectral emissivity of the SSA tends to the decrease, resulting in less power available for recovering per wavelength unit. Increasing the absorber operating temperature moves the black-body emitted power peaks towards shorter wavelength, increasing the recovering efficiency of the IR mirror at small width.

The recovered power extends the temperature range achievable by the MT-SSA, as shown in Fig. 7, where the efficiency is calculated for both an ideal and realistic IR mirror with $\lambda_{thres} = 2.2$ μm, considering as incident power 1000 W/m^2 and ambient temperature $T_{amb} = 20$ °C. On the basis of some already experimentally produced [41,42] or simulated [38] filters, four different values of Δ_{IRM} have been considered and results have been obtained for the absorber alone (dashed lines, Fig. 7) or for the whole collector (continuous lines). Since we choose a $\lambda_{thres} = 2.2$ μm the mirror starts to recover a noticeable fraction of power at temperature higher than 150°C and the efficiency of the absorber (neglecting the substrate and vessel) increases significantly up to about 450 – 500°C. At higher temperatures, particularly when substrate losses are neglected and large Δ_{IRM} are considered, there is a quick drop in efficiency due to increased power emitted at wavelengths lower than λ_{thres}.

As expected, the collector efficiency improves with increasing Δ_{IRM}, however a $\Delta_{IRM} = 2$ μm is sufficient to increase η_c from 30% to 46% at 350 °C and from 0 to 30% at 400 °C, whereas a 15% relative increase is obtained at 300 °C (from 50% to 58%).

3.3. Real IR mirror: results

Since it has already been shown that an optimized HVFP can be more efficient than concentrators up to 250 °C [43], we will focus our

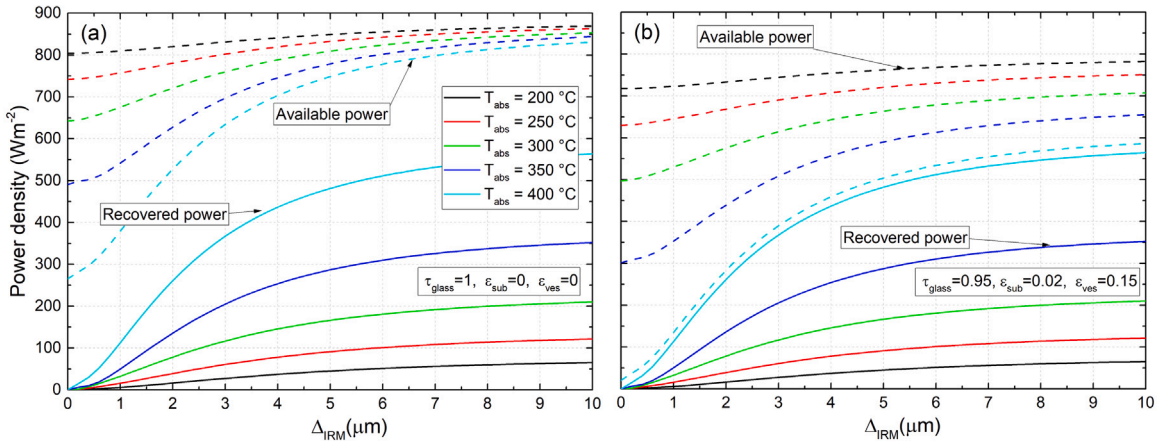

Fig. 6. Recovered (continuous lines) and available power (dashed lines) at different temperatures for (a) an MT-SSA absorber and (b) an HVFP collector with MT-SSA and an ideal mirror with different Δ_{IRM}.

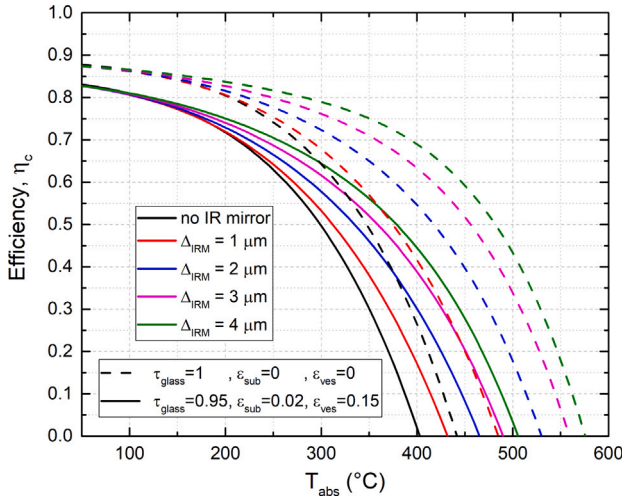

Fig. 7. Efficiency of an absorber with an ideal IR mirror designed at 300 °C and different Δ_{IRM}. Results refer to $I = 1000\,\mathrm{W/m^2}$ and $T_{amb} = 20$ °C, calculated for the absorber only (dashed lines) and the whole collector (continuous lines).

attention on the effect of a real IR mirror at temperatures equal or higher than 250 °C to extend the HVFP operational temperature range. To investigate this question in detail, we report colormaps representing the power loss of the couple absorber–glass in absence ($\Delta_{IRM} = 0\,\mu$m, Fig. 8(a)) or in presence of an IR mirror ($\Delta_{IRM} = 1, 2, 3, 4\,\mu$m, Fig. 8 (b), (c), (d), (e)) at different operating temperatures and for different reflectivity values ranging from 0.80 to 1. The power loss of the absorber through the glass can significantly be reduced by the presence of the IR mirror, in particular at T_{abs} above 350 °C. As expected, the higher the ρ_{IRM}, the greater the benefits in terms of recycled power.

The power losses are a fundamental parameter independent of the IR mirror transparency. We therefore studied the influence of all these parameters, Δ_{IRM}, ρ_{IRM} and τ_{IRM}, on the collector efficiency to determine their relative importance to the collector performance. These results are presented in Fig. 9, where colormaps of efficiency change with respect to these factors are shown: each row refers to different T_{abs}, whereas columns to different IR mirror bandwidth values. For each single figure, both transparency and reflectivity of the mirror have been varied in the range of 0.80 to 1.00. Of course, the higher the τ_{IRM} and ρ_{IRM} values for each rectangle, the higher the efficiency change. Nevertheless, non-negligible results can be obtained with realistic mirrors if certain values of τ_{IRM} and ρ_{IRM} are reached, as represented by the colored areas of Fig. 9, while the white areas are regions of non-positive efficiency change. Also, an important contribution in increasing the performance comes from the reflection bandwidth, in fact, increasing the Δ_{IRM} reduces the requirements on the transparency at the same temperature, as can be observed looking at the columns of Fig. 9. At temperatures of 250 °C and 300 °C one can register an efficiency change higher than zero for each of $\rho_{IRM} > 0.80$ and for each value of τ_{IRM} close to 1. On the contrary, reflectivity values close to 1 still need a high transparency. Therefore, in designing an IR mirror for mid temperature applications at nominal input power of $1000\,\mathrm{W/m^2}$, the priority has to be given to the mirror transparency and Δ_{IRM} more than reflectivity. Note that the collector efficiency values, η_c, in the legends of Fig. 9 are the ones calculated from Eq. (4) in absence of the IR mirror on the glass ($\rho_{IRM} = 0$). Therefore, to obtain the collector efficiency in presence of an IR mirror, one should also add the correspondent efficiency change value to η_c.

It is worth noting that the efficiency changes reported in Fig. 9 are peak efficiencies at $I = 1000\,\mathrm{W/m^2}$, whereas the power irradiated by the Sun on the earth varies accordingly to the seasons, the time of day, and the weather conditions. When the available power is lower than the nominal solar power, the efficiency change can be recalculated according to the formula:

$$\Delta\eta_x = \bar{\alpha}\tau_{glass}\left(1 - \tau_{IRM}\right)\left(\frac{I}{I_x} - 1\right) + \Delta\eta_{1000}\frac{I}{I_x}, \tag{7}$$

where $\Delta\eta_x$ is the efficiency change at Sun irradiance, $I_x = x\mathrm{W/m^2}$ and $\Delta\eta_{1000}$ is the efficiency change calculated at $1000\,\mathrm{W/m^2}$.

3.4. Monthly and annual energy conversion

When Eq. (7) is applied to Typical Meteorological Year Data (TMY) [44], we observe improvements in efficiency higher than those seen at the peak efficiency. We show the results obtained in two European cities as Naples[1] in Italy and Copenhagen[2] in Denmark, and in Phoenix in the United States.[3]

In Fig. 10(a,b,c) we report the monthly distribution of the converted energy at $T_{abs} = 250$ °C for the three chosen cities. The relative increase is more pronounced during winter particularly at higher latitude. Using a not ideal mirror with $\tau_{IRM} = 0.99$, and $\rho_{IRM} = 0.97$ produce still appreciable results.

[1] Lat.: $40°51'N$ Long.: $14°15'E$.
[2] Lat.: $55°41'N$ Long.: $12°35'E$.
[3] Lat.: $33°27'N$ Long.: $112°04'W$.

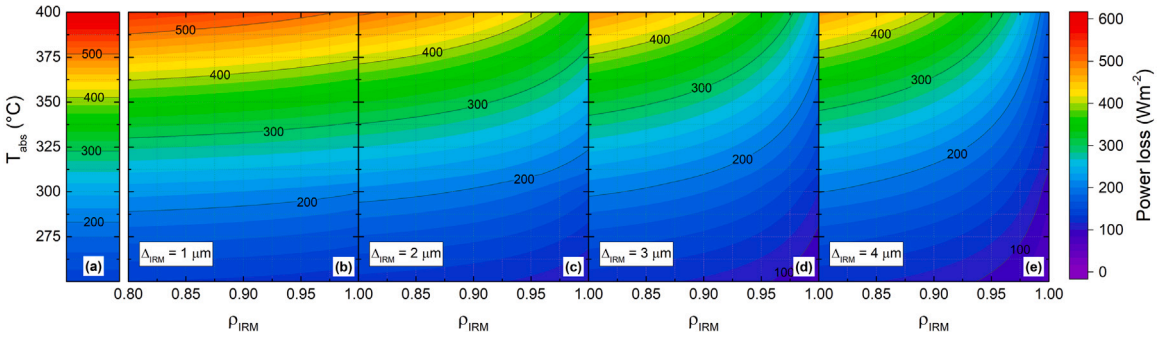

Fig. 8. Power loss of an HVFP collector equipped with a MT-SSA and an ideal IR mirror having different bandwidths: $\Delta_{IRM} = 0\,\mu m$ (a), 1 μm (b), 2 μm (c), 3 μm (d) 4 μm (e).

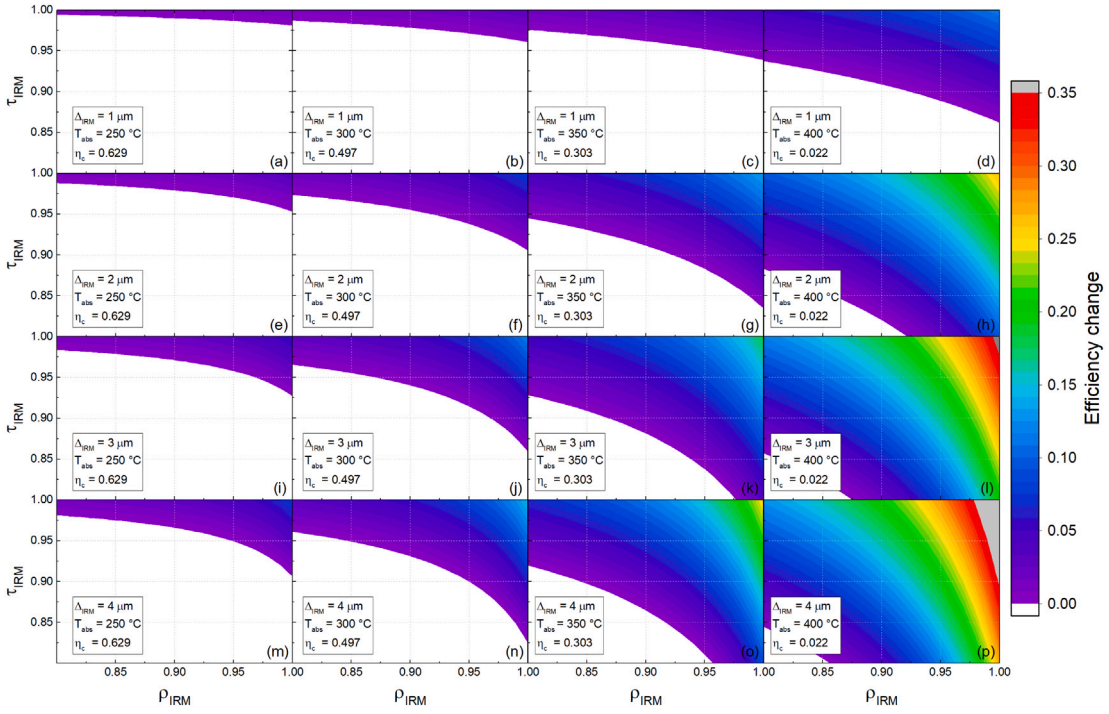

Fig. 9. Efficiency change of a collector equipped with an MT-SSA and possible realistic mirrors with Δ_{IRM} from 1 (top row) to 4 μm (bottom row) at different temperatures, from 250 °C (left column) to 400 °C (right column), as function of mirror reflectivity and transmissivity. $I = 1000\,W/m^2$, $T_{amb} = 20$ °C and radiative losses from the envelope have been assumed in the calculation.

In Copenhagen the use of the IR mirror allows to extend the useful hours during the days at high temperatures, however at such high latitudes during autumn and winter the Sun is too low on the horizon for too few hours to reach the 250 °C working temperature. Still, other applications at lower temperatures (such as district heating) could use the heat generated by the HVFP during winter.

When integrating over the year, we observe that a peak efficiency change due to the IR ideal mirror ($\Delta_{IRM} = 2\,\mu m$, $\tau_{IRM} = 1$, and $\rho_{IRM} = 1$) for working temperature of 250 °C of 3.9% results in a 14.7% increase of produced annual energy in Naples (from $3044\,MJ/m^2$ to $3493\,MJ/m^2$, see Fig. 10(d)). The same peak efficiency changes produce a relative annual energy increase of 21.4% in Copenhagen (bringing the available energy from $1452\,MJ/m^2$ to $1762\,MJ/m^2$, and 10.6% in Phoenix (available energy from $4555\,MJ/m^2$ to $5038\,MJ/m^2$) with an annual efficiency that increases from 0.517 up to 0.572. At higher temperature the radiative losses increase and the same bandwidth of the ideal mirror can recover more energy (see Fig. 10(e,f)), extending the operating temperature range of the panel. However the losses can became so important that the bandwidth should be extended to produce a significant amount of annual energy. At 300 °C an ideal mirror with $\Delta_{IRM} = 3\,\mu m$ would bring the annual energy from $3063\,MJ/m^2$ to $4363\,MJ/m^2$ in Phoenix, with a relative improvement of 42% and an annual efficiency of 49.5%, and from $1731\,MJ/m^2$ to $2871\,MJ/m^2$ in Naples, with a relative increase of 65.9% and an annual efficiency of 41.8%. At the same temperature of 300 °C, if we consider instead a realistic mirror with $\Delta_{IRM} = 3\,\mu m$, $\tau_{IRM} = 0.99$, and $\rho_{IRM} = 0.97$, the annual efficiency varies from 25.2% to 36.1% in Naples, from 34.8% to 44.3% in Phoenix, and from 13.7% to 23.8% in Copenhagen.

Note that data from Ref. [44] are hourly-mean value for each month, which averages any combination of sunny and cloudy days and leads to an underestimation of the monthly output. Indeed, if one could shut down the system during the days when the light is not enough, one might increase the available energy, which be an appropriate optimization problem for future studies.

4. Conclusions and perspectives

In this work, we considered the problem of reducing losses for solar thermal devices to improve their overall efficiencies. The concept investigated was to introduce a selective infrared (IR) mirror to recapture part of the radiated heat from the system through the photon

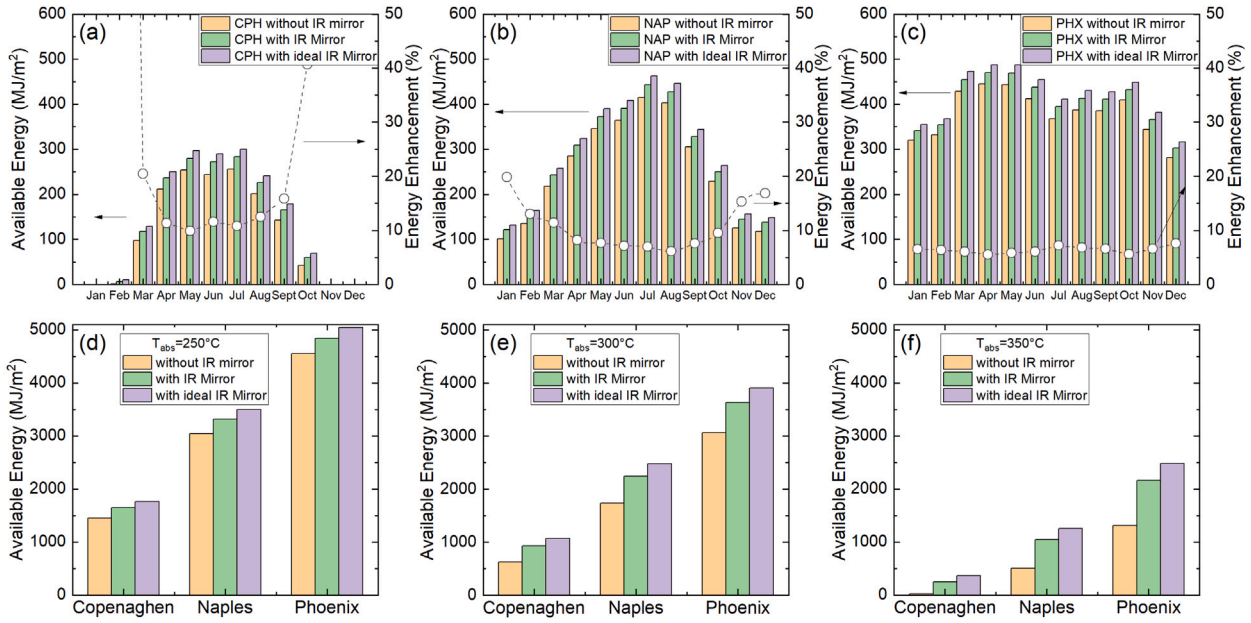

Fig. 10. Upper row: Monthly converted energy for a HVFP working at 250 °C in the caso of no IR mirror, realistic IR mirror ($\Delta_{IRM} = 2\,\mu m$, $\tau_{IRM} = 0.99$, and $\rho_{IRM} = 0.97$) and ideal IR mirror with $\Delta_{IRM} = 2\,\mu m$ (left-hand axis), and monthly percentage of the energy enhancement obtained with the real IR mirror (right-hand axis). Lower row: Converted annual energy at different operating temperature: 250 °C (d), 300 °C (e) and 350 °C (f). The analysis has been performed for three cities: (a) Copenhagen (DK), (b) Naples (IT) and (c) Phoenix (AZ).

recycling mechanism. To understand the performance, we modeled both the optical and thermal equilibrium for a range of designs. Our models show that an appropriately chosen IR mirror can extend the operating temperature range, as well as improve the panel efficiency at a fixed working temperature. An effective IR mirror with bandwidth $\Delta_{IRM} = 3\,\mu m$, and reflectivity $\rho_{IRM} = 0.97$ can reduce the power loss below $300\,W\,m^{-2}$ at temperatures up to 350 °C, resulting in efficiencies higher than 50% at solar irradiance of $1000\,W/m^2$. The results indicate that the efficiency can be improved for limited values of the mirror transmittance only, and it is particularly important at temperature equal or below 300 °C. At higher temperatures the emitted power increases and the reflectance gains importance over transmittance. The bandwidth of the mirror is important; still, $\Delta_{IRM} = 1\,\mu m$ is already enough to have a measurable improvement at temperatures above 250 °C. For instance, a bandwidth $\Delta_{IRM} = 3\,\mu m$ with transparency $\tau_{IRM} = 0.99$, and reflectivity $\rho_{IRM} = 0.97$ can lead to a relative annual efficiency improvement of the order of 50% in Phoenix at 300 °C. These results indicate that it is significantly beneficial to design and realize IR mirrors with the aim of improving the high vacuum flat solar thermal panel efficiency in the mid temperature range (250 °C–350 °C). Such temperatures and efficiencies open a path towards the use of Solar energy in a large number of industrial applications requiring heat. In particular, high-pressure steam generation represents a large fraction of current industrial heat demand that has not yet been addressed by widespread renewable energy solutions commercially. Such improvements become more interesting considering that the easy installation of high vacuum flat solar thermal panels on flat roofs can save land area usage, which is particularly valuable in European countries and other high population density countries.

CRediT authorship contribution statement

Carmine D'Alessandro: Methodology, Software. **Davide De Maio:** Methodology, Software. **Marilena Musto:** Supervision. **Daniela De Luca:** Data curation, Writing - original draft, Writing - review & editing. **Emiliano Di Gennaro:** Supervision, Visualitation, Writing - review & editing. **Peter Bermel:** Supervision, Writing - review & editing. **Roberto Russo:** Conceptualization, Writing - review & editing.

Declaration of competing interest

The authors declare that they have no known competing financial interests or personal relationships that could have appeared to influence the work reported in this paper.

Acknowledgments

The Ph.D. grant of one of the authors (DDL) is funded by the PON2014-2020, Italy "Dottorati innovativi con caratterizzazione industriale, XXXIV ciclo" program. The Ph.D. grant of one of the authors (DDM) is funded by the CNR-Confindustria, Italy "Dottorati di Ricerca Industriali" program XXXIV ciclo. We also acknowledge support from the Department of Energy, USA (grant DE-EE0004946), the National Science Foundation, USA (grants EEC1454315-CAREER, EEC-1227110, and CBET-1855882), and the Office of Naval Research, USA (grants N000014-15-1-2833 and N00014-19-S-B001).

References

[1] Chapman AJ, McLellan BC, Tezuka T. Prioritizing mitigation efforts considering co-benefits, equity and energy justice: Fossil fuel to renewable energy transition pathways. Appl Energy 2018;219:187–98. http://dx.doi.org/10.1016/j.apenergy.2018.03.054, URL https://linkinghub.elsevier.com/retrieve/pii/S0306261918303830.

[2] Lauterbach C, Schmitt B, Jordan U, Vajen K. The potential of solar heat for industrial processes in Germany. Renew Sustain Energy Rev 2012;16(7):5121–30. http://dx.doi.org/10.1016/j.rser.2012.04.032, URL https://linkinghub.elsevier.com/retrieve/pii/S1364032112003073.

[3] Shahsavari A, Akbari M. Potential of solar energy in developing countries for reducing energy-related emissions. Renew Sustain Energy Rev 2018;90:275–91. http://dx.doi.org/10.1016/j.rser.2018.03.065, URL https://linkinghub.elsevier.com/retrieve/pii/S1364032118301527.

[4] Kranzl L, Hartner M, Müller A, Resch G, Fritz S, Fleiter T, et al. Heating and cooling outlook until 2050, EU-28. 2018, URL https://www.hotmaps-project.eu/wp-content/uploads/2018/05/Hotmaps_D5-2_v16_2019-03-01.pdf.

[5] Bhatia SC. Advanced renewable energy systems | ScienceDirect. 2014, URL https://www.sciencedirect.com/book/9781782422693/advanced-renewable-energy-systems.

[6] Kennedy CE. Review of mid- to high-temperature solar selective absorber materials. Tech. rep. NREL/TP-520-31267, 15000706, U.S. Department of Energy Office of Scientific and Technical Information; 2002, http://dx.doi.org/10.2172/15000706, URL http://www.osti.gov/servlets/purl/15000706-1i6DGF/native/.

[7] Bermel P, Lee J, Joannopoulos JD, Celanovic I, Soljacie M. Selective solar absorber. Ann Rev Heat Transf 2012;15:231–54. http://dx.doi.org/10.1615/AnnualRevHeatTransfer.2012004119.

[8] Burlafinger K, Vetter A, Brabec CJ. Maximizing concentrated solar power (CSP) plant overall efficiencies by using spectral selective absorbers at optimal operation temperatures. Sol Energy 2015;120:428–38. http://dx.doi.org/10.1016/j.solener.2015.07.023, URL https://linkinghub.elsevier.com/retrieve/pii/S0038092X1500393X.

[9] Weinstein LA, Loomis J, Bhatia B, Bierman DM, Wang EN, Chen G. Concentrating solar power. Chem Rev 2015;115(23):12797–838. http://dx.doi.org/10.1021/acs.chemrev.5b00397, URL https://pubs.acs.org/doi/10.1021/acs.chemrev.5b00397.

[10] D'Alessandro C, De Maio D, De Luca D, Di Gennaro E, Gioffrè M, Iodice M, et al. Solar selective coating for thermal applications. Key Eng Mater 2019;813:316–21, URL https://www.scientific.net/KEM.813.316.

[11] Sergeant NP, Pincon O, Agrawal M, Peumans P. Design of wide-angle solar-selective absorbers using aperiodic metal-dielectric stacks. Opt Express 2009;17(25):22800. http://dx.doi.org/10.1364/OE.17.022800, URL https://www.osapublishing.org/oe/abstract.cfm?uri=oe-17-25-22800.

[12] Guo H-X, He C-Y, Qiu X-L, Shen Y-Q, Liu G, Gao X-H. A novel multilayer high temperature colored solar absorber coating based on high-entropy alloy MoNbHfZrTi: Optimized preparation and chromaticity investigation. Sol Energy Mater Sol Cells 2020;209:110444. http://dx.doi.org/10.1016/j.solmat.2020.110444, URL https://linkinghub.elsevier.com/retrieve/pii/S0927024820300507.

[13] Cao F, McEnaney K, Chen G, Ren Z. A review of cermet-based spectrally selective solar absorbers. Energy Environ Sci 2014;7(5):1615. http://dx.doi.org/10.1039/c3ee43825b, URL http://xlink.rsc.org/?DOI=c3ee43825b.

[14] Cao F, Kraemer D, Sun T, Lan Y, Chen G, Ren Z. Enhanced thermal stability of W-Ni-Al_2O_3 cermet-based spectrally selective solar absorbers with tungsten infrared reflectors. Adv Energy Mater 2015;5(2):1401042. http://dx.doi.org/10.1002/aenm.201401042, URL http://doi.wiley.com/10.1002/aenm.201401042.

[15] Lampert CM. Coatings for enhanced photothermal energy collection I. Selective absorbers. Solar Energy Mater 1979;1(5–6):319–41. http://dx.doi.org/10.1016/0165-1633(79)90001-7, URL https://linkinghub.elsevier.com/retrieve/pii/0165163379900017.

[16] Okuyama M, Saji K, Adachi T, Okamoto H, Hamakawa Y. Selective absorber using glow-discharge amorphous silicon for solar photothermal conversion. Solar Energy Mater 1980;3(3):405–13. http://dx.doi.org/10.1016/0165-1633(80)90029-5, URL https://linkinghub.elsevier.com/retrieve/pii/0165163380900295.

[17] Donnadieu A, Seraphin BO. Optical performance of absorber–reflector combinations for photothermal solar energy conversion. J Opt Soc Amer 1978;68:292–7. http://dx.doi.org/10.1364/JOSA.68.000292.

[18] Huang MH, Mao S, Feick H, Yan H, Wu Y, Kind H, et al. Room-temperature ultraviolet nanowire nanolasers. Science, New Ser 2001;292(5523):1897–9, URL http://www.jstor.org/stable/3083931.

[19] Zhu J, Yu Z, Burkhard GF, Hsu C-M, Connor ST, Xu Y, et al. Optical absorption enhancement in amorphous silicon nanowire and nanocone arrays. Nano Lett 2009;9(1):279–82. http://dx.doi.org/10.1021/nl802886y, URL https://pubs.acs.org/doi/10.1021/nl802886y.

[20] Celanovic I, Jovanovic N, Kassakian J. Two-dimensional tungsten photonic crystals as selective thermal emitters. Appl Phys Lett 2008;92(19):193101. http://dx.doi.org/10.1063/1.2927484, URL http://aip.scitation.org/doi/10.1063/1.2927484.

[21] Li P, Liu B, Ni Y, Liew KK, Sze J, Chen S, et al. Large-scale nanophotonic solar selective absorbers for high-efficiency solar thermal energy conversion. Adv Mater 2015;27(31):4585–91. http://dx.doi.org/10.1002/adma.201501686, URL http://doi.wiley.com/10.1002/adma.201501686.

[22] Woolf D, Hensley J, Cederberg JG, Bethke DT, Grine AD, Shaner EA. Heterogeneous metasurface for high temperature selective emission. Appl Phys Lett 2014;105(8):081110. http://dx.doi.org/10.1063/1.4893742, URL http://aip.scitation.org/doi/10.1063/1.4893742.

[23] Khan MR, Wang X, Sakr E, Alam MA, Bermel P. Enhanced selective thermal emission with a meta-mirror following Generalized Snell's Law. MRS Proc 2015;1728. http://dx.doi.org/10.1557/opl.2015.357, URL https://www.cambridge.org/core/product/identifier/S1946427415003577/type/journal_article.

[24] Zhou Z, Tian H, Hymel TM, Reddy H, Shalaev VM, Cui Y, et al. High-temperature, spectrally-selective, scalable, and flexible thin-film Si absorber and emitter. Opt Mater Express 2020;10(1):208–21. http://dx.doi.org/10.1364/OME.381680, URL https://www.osapublishing.org/ome/abstract.cfm?uri=ome-10-1-208.

[25] De Maio D, D'Alessandro C, Caldarelli A, Musto M, De Luca D, Di Gennaro E, et al. Efficiency of selective solar absorber in high vacuum flat solar thermal panels: The role of emissivity and cut-off wavelength. 2020, Preprints. http://dx.doi.org/10.20944/preprints202008.0162.v2.

[26] https://alanod.com/.

[27] Grena R. Efficiency gain of a solar trough collector due to an IR-reflective film on the non-irradiated part of the receiver. Int J Green Energy 2011;8(7):715–33. http://dx.doi.org/10.1080/15435075.2011.602154, URL http://www.tandfonline.com/doi/abs/10.1080/15435075.2011.602154.

[28] Cyulinyana MC, Ferrer P. Heat efficiency of a solar trough receiver with a hot mirror compared to a selective coating. S Afr J Sci 2011;107(11/12). URL http://www.scielo.org.za/scielo.php?script=sci_arttext&pid=S0038-23532011000600010.

[29] Kaluba VS, Ferrer P. A model for hot mirror coating on solar parabolic trough receivers. J Renew Sustain Energy 2016;8(5):053703. http://dx.doi.org/10.1063/1.4965252, URL http://aip.scitation.org/doi/10.1063/1.4965252.

[30] TVP Solar, URL https://www.tvpsolar.com/.

[31] Ilic O, Bermel P, Chen G, Joannopoulos JD, Celanovic I, Soljačić M. Tailoring high-temperature radiation and the resurrection of the incandescent source. Nature Nanotechnol 2016;11(4):320–4. http://dx.doi.org/10.1038/nnano.2015.309, URL http://www.nature.com/articles/nnano.2015.309.

[32] Fan JCC, Bachner FJ. Transparent heat mirrors for solar-energy applications. Appl Opt 1976;15(4):1012. http://dx.doi.org/10.1364/AO.15.001012, URL https://www.osapublishing.org/abstract.cfm?URI=ao-15-4-1012.

[33] Mohamad K, Ferrer P. Parabolic trough efficiency gain through use of a cavity absorber with a hot mirror. Appl Energy 2019;238:1250–7. http://dx.doi.org/10.1016/j.apenergy.2019.01.163, URL https://linkinghub.elsevier.com/retrieve/pii/S0306261919301643.

[34] D'Alessandro C, De Maio D, De Luca D, Musto M, Di Gennario E, Rotondo G, et al. Measurements of spectrally averaged absorptivity and emissivity for a selective solar absorber in high vacuum under direct solar illumination. J Phys: Conf Ser 2020;1599. http://dx.doi.org/10.1088/1742-6596/1599/1/012027.

[35] Bejan A, Kraus AD. Heat transfer handbook. Wiley; 2003, URL https://www.wiley.com/en-us/Heat+Transfer+Handbook-p-9780471390152.

[36] Carniglia CK. Comparison of several shortwave pass filter designs. Appl Opt 1989;28(14). http://dx.doi.org/10.1364/AO.28.002820.

[37] https://www.thorlabs.com/newgrouppage9.cfm?objectgroup_id=139.

[38] De Luca D, Russo R, Di Gennaro E, Bermel P. Rugate filter window coating for improvement of vacuum solar thermal absorber efficiencies. In: Proc. SPIE 11496, new concepts in solar and thermal radiation conversion III. 2020, http://dx.doi.org/10.1117/12.2574604, URL https://www.spiedigitallibrary.org/conference-proceedings-of-spie/11496/2574604/Rugate-filter-window-coating-for-improvement-of-vacuum-solar-thermal/10.1117/12.2574604.short?SSO=1.

[39] De Maio D, D'Alessandro C, De Luca D, Musto M, Di Gennario E, Rotondo G, et al. Thermal efficiency of a concentrating solar collector under high vacuum. J Phys: Conf Ser 2020;1599. http://dx.doi.org/10.20944/preprints202001.0072.v1.

[40] Xu K, Hao L, Du M, Mi J, Yu Q, Li S, et al. Thermal emittance of Ag films deposited by magnetron sputtering. Vacuum 2020;174. http://dx.doi.org/10.1016/j.vacuum.2020.109200.

[41] Kontio JM, Simonen J, Leinonen K, Kuittinen M, Tapio N. Broadband infrared mirror using guided-mode resonance in a subwavelength germanium grating. Opt Lett 2010;35(15). http://dx.doi.org/10.1364/OL.35.002564, URL https://www.osapublishing.org/ol/abstract.cfm?uri=ol-35-15-2564.

[42] Foley JM, Itsuno AM, Das T, Velicu S, Phillips JD. Broadband long-wavelength infrared Si/SiO_2 subwavelength grating reflector. Opt. Lett. 2012;37(9). http://dx.doi.org/10.1364/OL.37.001523, URL https://www.osapublishing.org/ol/abstract.cfm?uri=ol-37-9-1523.

[43] Moss R, Henshall P, Arya F, Shire G, Hyde T, Eames P. Performance and operational effectiveness of evacuated flat plate solar collectors compared with conventional thermal, PVT and PV panels. Appl Energy 2018;216:588–601. http://dx.doi.org/10.1016/j.apenergy.2018.01.001, URL https://linkinghub.elsevier.com/retrieve/pii/S0306261918300011.

[44] JRC photovoltaic geographical information system (PVGIS) - European commission. 2020, URL https://re.jrc.ec.europa.eu/pvg_tools/it/#DR.